Chemical Engineering Journal 499 (2024) 156262

Contents lists available at ScienceDirect

Chemical Engineering Journal

journal homepage: www.elsevier.com/locate/cej

Mechanisms and valorization of selective adsorption of Sb(III) by amino-functionalized lignin-based porous biochar

Wei Huang [a], Zhixuan Yang [a], Junguang Hu [a], Xin Chen [a], Wei Li [a], Zhiguo Wang [a], Chun Zhang [a], Qiongchao Wang [a], Xinxin Xiao [b,*], Peng Yu [a,*]

[a] School of Chemistry and Materials Science, Hunan Agricultural University, Changsha, Hunan 410128, China
[b] Department of Chemistry and Bioscience, Aalborg University, Fredrik Bajers Vej 7H, 9220 Aalborg East, Denmark

ARTICLE INFO

Keywords:
Biochar
Trivalent antimony
Selective adsorption
Removal mechanism
Valorization

ABSTRACT

Antimony contamination in aquatic environment raises tremendous concerns for human health and ecosystem safety, while there is a lack of methods for efficient and selective adsorption of antimony. In this study, an adsorbent for trivalent antimony (Sb(III)) removal is obtained by cross-linking polyethyleneimine (PEI) onto phosphoric acid-modified lignin-based porous biochar (PPLB). PPLB exhibits efficient adsorption of Sb(III) with a maximum value of 371.7 mg/g, which is also highly selective as the Sb(III) removal capability by PPLB remains unaffected under the common co-existing anions (Cl^-, NO_3^-, PO_4^{3-}, and CO_3^{2-}) and less affected with the co-existing cations (Cd^{2+}, Zn^{2+}, Cu^{2+}, and Pb^{2+}). Such a performance is validated in three simulated Sb(III)-contaminated water bodies (Zijiang River water, industrial wastewater, and mining area water). Understanding of the adsorption mechanisms is further established via density functional theory calculations, revealing the dominant adsorption site of Sb(III) on PPLB is –NH- groups. It's finally concluded that the removal of Sb(III) by PPLB is governed by complexation, with also the contribution from ligand exchange and hydrogen bonding. As a proof of concept, the spent PPLB adsorbed with Sb(III) is valorized into an active material of sodium ion battery, demonstrating a specific capacity of 192.4 mA h/g for 1000 cycles with a good long-term stability.

1. Introduction

Antimony (Sb) contamination in aquatic environment is increasingly concerning due to the rapid expansion of industrial activities such as mining and smelting processes, flame retardants, pharmaceutical production and so on [1–3]. Sb exists primarily as Sb(III) and Sb(V), with Sb (III) known for its higher mobility and toxicity over Sb(V). The former has been demonstrated to cause metabolic disorders and organ damage, with a particular propensity to the nervous system, thus a considerable threat to human health and ecosystem [4]. Currently, the concentration of Sb in the mining wastewater of Xikuangshan in China was reported to be 2 to 6384 μg/L [5], considerably higher than the standard upper limit of 5 μg/L [6]. Besides, Antimony contamination of groundwater in Norway reaches 50 mg/L [7]. During Sb mining process, Sb-containing wastewater gradually becomes extremely acidic (pH<3) due to the combination of acidic reagents and microorganisms, leading to numerous environmental issues [8]. It is therefore imperative to develop treatment methods for Sb-contaminated wastewater. Among various available methods, adsorption features great economic efficiency and easy operation [9].

Currently, various adsorbents, especially carbon materials and their composites, have been developed for the remediation of Sb(III) contamination. For instance, Wang et al. described Fe-modified biochar (FeBC) with a maximum adsorption of 64.0 mg/g for Sb(III). The iron-active components (Fe_3O_4) and inherent C=O bonds within the material enhanced Sb(III) adsorption synergistically with the assistance of peroxymonosulfate [10]. Hou and co-workers prepared cerium-doped sulfur-carbon aerogel (Ce@SCA), achieving a maximum Sb(III) adsorption of 345.2 mg/g. The elimination of Sb(III) was mainly facilitated through the redox and complexation effects of cerium [11]. However, the utilization of transition metal materials to remove Sb suffers from leaching of metal ions, and the subsequent decay of adsorbent stability and even secondary pollution [12]. Metal-free carbon-based adsorbents possess great chemical stability, good cost efficiency and environmental friendliness, which are attracting extensive attention for Sb(III) removal [13]. For example, Shen et al. proposed a chitosan modified

* Corresponding authors.
E-mail addresses: xixi@bio.aau.dk (X. Xiao), pengy7505@hunau.edu.cn (P. Yu).

https://doi.org/10.1016/j.cej.2024.156262
Received 4 September 2024; Received in revised form 27 September 2024; Accepted 27 September 2024
Available online 29 September 2024

nicotinamide-modified eupatorium adenophorum biochar, exhibiting a maximum Sb(III) adsorption of 170.15 mg/g, considerably higher than that of unmodified biochar (9.97 mg/g). The introduced hydroxyl (–OH) and carbonyl (C=O) groups on the adsorbent after molecular modification synergistically facilitated the absorption of Sb(III) [14]. Thus, surface modification of carbon-based adsorbents can modulate their surface structure and provide specific functional groups for enhanced Sb (III) removal [15,16]. Given that Sb is a critical industrial metal, the selective adsorption of antimony is another important criterion for economic effectiveness. However, there is still a lack of investigation on the selective Sb adsorption by carbon-based adsorbents. Lignin, a widely available biomass with rich surface functional groups (–OH, C=O, etc.), could serve as a potential carrier for the remediation of heavy metal [17–19]. As far as we know, lignin-based biochar has not yet been reported for the selective adsorption of Sb(III).

Polyethyleneimine (PEI), a representative polymer with numerous amino groups (–NH_2, –NH-, and −N=), displays a pronounced selective adsorption ability for heavy metals [20–22]. For example, Chen and coworkers reported a PEI modified zero-valent iron composite using tannic acid as the stabilizer, demonstrating a highly selective Cr(VI) adsorption under the coexistence of Cu(II), Ni(II), and Pb(II), with a maximum Cr (VI) adsorption of 161.6 mg/g. The high adsorption ability and selectivity of Cr(VI) were mainly ascribed to the efficient electrostatic attraction between protonated amino groups from PEI and Cr(VI), and the complexation of the amino group with Cr(VI) [23]. Besides, Li et al. found that PEI modified chitosan/tailings composite exhibited selective adsorption for Pb(II) and Cd(II) than other metals such as Zn(II), Mg(II), Mn(II) and Al(III), with the mechanisms of adsorption attributed to the synergistic effects of –NH_2, Si–O, and –OH groups [24]. We thus propose to introduce PEI molecules onto the lignin-based biochar to achieve the selective adsorption of Sb(III) undergoing complexation between amino groups and Sb(III). The comprehensive understanding on the underline mechanisms is still missing.

This study therefore seeks to explore the potential application of PEI-modified lignin-based porous biochar (PPLB) for the selective adsorption of Sb(III). Surface morphology and crystalline natures of the prepared PPLB are characterized. The influence factors (initial solution pH, dosage, and initial concentration of Sb(III)) on Sb(III) elimination, the effect of coexisting ions, and the reusability of PPLB are then systematically studied. The selective adsorption ability of Sb(III) by PPLB is also confirmed in real water bodies under the coexistence of different cations. The interaction between amino groups (–NH_2, –NH-, and −N=) and Sb(III) is quantified by density functional theory (DFT) calculations. Thus, the new insight into selective adsorption of Sb(III) by amino-functionalized lignin-based porous biochar is established. Further, as a proof of concept, the spent PPLB adsorbed with Sb(III) adsorbent is valorized as an anode active material for sodium ion batteries (SIBs).

2. Chemicals and methods

2.1. Chemicals

Potassium antimony tartrate hemihydrate ($KSbO_4H_4O_7{\cdot}1/2H_2O$, 99.0 %), phosphoric acid (H_3PO_4, 85.1 %), hydrochloric acid (HCl, 36.0–38.0 %), sodium hydroxide (NaOH, 96.0 %), branched polyethyleneimine (PEI, molecular weight = 1800, 99.0 %), glutaraldehyde ($C_5H_8O_2$, 25 %), potassium hydroxide (KOH, 99.0 %), and lignin (dealkalized) were all supplied by Sinopharm Chemical Reagent Co., Ltd. All chemicals were used as received without further purification.

2.2. Synthesis of adsorbents

Lignin samples were first impregnated in H_3PO_4 solution (85.1 wt%) at a mass ratio of 1:5, and dispersed in 60 mL ultrapure water. The aqueous mixture was stirred at 85 °C for 2 h, then heated at 150 °C to evaporate excess water, forming a homogenous slurry. The slurry in a porcelain boat was then heated in a microwave tube furnace at 500 °C under Ar atmosphere for 2 h. After cooling, the sample was washed with ultrapure water until neutral pH was obtained and then dried at 60 °C for 12 h. The phosphoric acid-activated lignin-based porous biochar (PLB) was yielded for subsequent use.

0.5 g PLB was added to a 30 mL PEI solution (15 % (w/v)) and stirred at 30 °C with 300 rpm for 24 h. The mixed solution was then immediately transferred to a 100 mL 1 % (w/v) glutaraldehyde solution for crosslinking, and stirred at 30 °C for 30 min. The resulting sample was washed and dried at 60 °C for 12 h. Finally, the PEI-modified PLB (PPLB) samples were obtained.

2.3. Characterization

The surface features and elemental composition of the synthesized adsorbents were analyzed using a field emission scanning electron microscopy (FESEM, ZEISS Sigma 300, Germany) equipped with an energy dispersive X-ray spectroscopy (EDS) detector. Fourier transform infrared spectroscopy (FTIR, Bruker ALPHA, Germany) was employed to visualize the functional groups on the materials. Brunauer-Emmett-Teller (BET, JW-BK100, China) method was used to analyze the specific surface area and porous structure. X-ray diffraction (XRD, SHIMADZU 6000, Japan) and X-ray photoelectron spectroscopy (XPS, Thermo Scientific K-Alpha, USA) were utilized to examine the elemental composition, ratio, and chemical states in the materials. Finally, inductively coupled plasma optical emission spectrometry (ICP-OES, Thermo Fisher iCAP7200 HS, UK) was used to measure the concentration of Sb(III) in the solution.

2.4. Batch experiments

Sb(III) stock solution (1000 mg/L) was prepared by dissolving $KSbO_4H_4O_7{\cdot}1/2H_2O$ in ultrapure water, and all test solutions were diluted from this stock. Typical batch tests were performed in conical flasks with 200 mL Sb(III) solution (50 mg/L), with an adsorbent dosage of 0.25 g/L. The initial solution pH (pH_0) was adjusted using 0.1 mol/L HCl or NaOH. The flasks were put in a thermostatic shaker at 25 °C and 220 r/min. Aliquots of reactive solution were taken at various time points (5, 10, 15, 30, 45, 60, and 120 min) and filtered by a 0.45 μm filter membrane. The equilibrium concentration of Sb was measured using ICP-OES. All data were collected via three duplicates. More details regarding the batch experiments, the point of zero charge (pH_{pzc}), analysis of adsorption model, and the regeneration of the PPLB are provided in Text S1, S2, S3, and S4, respectively.

2.5. Practical applicability of PPLB

To evaluate the practicality of PPLB in wastewater treatment, three types of water (Zijiang River water, industrial wastewater, and mining area water) were used as simulated wastewater by adding a specific concentration of $KSbO_4H_4O_7{\cdot}1/2H_2O$. 50 mg of PPLB was added to 200 mL of wastewater and shaken for 2 h. All experiments were conducted at room temperature to analyze the actual Sb(III) removal behaviors using ICP-OES.

2.6. Computational methods

Density functional theory (DFT) calculations were conducted using the VASP code [25,26]. For the geometry optimization of isolated molecules, plane-wave DFT calculations were employed using projector augmented wave (PAW) pseudopotentials and the generalized gradient approximation (GGA) of Perdew–Burke–Ernzerhof (PBE). Electron-ion interactions were described using a plane wave basis with an energy cutoff of 400 eV and a Γ-only k-point. Atomic relaxations continued until the residual forces were less than 0.01 eV/Å, and the energy during self-consistent field (SCF) cycles converged to 10^{-5} eV. A vacuum layer of 10

Å was introduced in the x, y, and z directions, sufficient to prevent interactions through the boundary. The optimized geometries were used for single point calculation to determine the total energy.

2.7. Electrochemical measurements

The spent PPLB samples adsorbed with Sb(III) were recycled and converted to Sb/C composites by annealing at 500 °C under Ar atmosphere for 2 h. A slurry was prepared by dissolving a mixture of Sb/C composite (80 wt%), super P (10 wt%) and polyvinylidene fluoride (PVDF, 10 wt%) in N-methyl-2-pyrrolidone (NMP). The resulting slurry was uniformly coated onto a copper foil to prepare the working electrode. The counter electrode was sodium metal. The electrolyte employed was 1.0 M $NaClO_4$ dissolved in a mixed solvent (100: 5 vol%) comprising propylene carbonate (PC) and fluoroethylene carbonate (FEC). The assembled CR2032 half-coin cells were measured by galvanostatic charge–discharge (GCD) in a voltage window of 0.01–3.0 V controlled by a Neware testing system (Shenzhen Neware Electronic Co.), in an argon-filled glovebox at room temperature.

3. Results and discussion

3.1. Surface morphology and crystalline natures

The morphology and elemental composition of PLB and PPLB are examined using scanning electron microscopy (SEM). As shown in Fig. 1a, PLB displays a rough surface with a uniform distribution of pores. After PEI modification (Fig. 1b), PPLB shows no obvious change on the porous structure in comparison to that of PLB, implying that the introduction of PEI molecules retains the initial structure of PLB. As seen from the EDS mapping images of PPLB (Fig. 1c-f), elemental C, O, P, and N are homogeneously distributed on the sample, with a nitrogen content reaching 11.39 wt% (Fig. S1), verifying the successful grafting of PEI onto the skeleton of PPLB.

The crystalline structures of PLB and PPLB are characterized using XRD (Fig. 2a). PLB sees a broad diffraction peak at $2\theta = 25.3°$ related to the (0 0 2) crystalline plane, and the peak located at $2\theta = 43.1°$ representing the (1 0 0) crystalline plane, indicating an amorphous carbon structure. In comparison to that of PLB, the (0 0 2) peak diffraction angle of PPLB is slightly negatively shifted, likely due to the insertion of PEI, causing an increase in interlayer spacing of carbon [27]. Meanwhile, FTIR spectra (Fig. 2b) sharply exhibit the signals of surface functional groups of PLB and PPLB within 4000–400 cm^{-1}. The broad peak at 3445 cm^{-1} is primarily assigned to overlapping vibrations of –OH, $–NH_2$, and –NH- groups, indicative of the presence of adsorbed H_2O and amino groups on the PPLB surface [28]. The bending vibration peak at 1445 cm^{-1} is assigned to the –NH- signal of PEI molecules, which is not seen from that of PLB, confirming the successful modification of the PPLB surface with PEI [29]. The stretching vibration peak at 1640 cm^{-1} corresponding to C=O, while the peaks at 1154 and 1032 cm^{-1} attributed to P=O stretching and P-O vibrations, respectively, are found from both samples, verifying the successful introduction of phosphorus-containing groups on the material surface after H_3PO_4 activation [30]. Notably, an enhanced vibration peak intensity at 1385 cm^{-1} corresponding to the stretching vibrations of C-N/C-P is seen on PPLB. After PEI modification, the attenuation of P=O/P-O peaks and the amplification of C-N/C-P vibrations indicate that PEI molecules bind to phosphorus-containing groups.

The N_2 adsorption–desorption isotherms and pore-size distributions of PLB (Fig. 2c) and PPLB (Fig. 2d) are analyzed. According to International Union of Pure and Applied Chemistry (IUPAC), the adsorption–desorption isotherms of both samples exhibit type IV with H3 hysteresis loops, indicating PLB and PPLB possess the features of mesoporous structure [31]. The pore-size distribution plots (insets of Fig. 2c and 2d) reveal that both samples exhibit multi-scale pores with a hierarchical structure comprising micropores and mesopores. The average pore size of PLB is 6.7 nm, which increases to 9.0 nm after PEI modification for PPLB. The pore volume is reduced from 1.3 to 0.7 cm^3/g. In contrast to PLB, PPLB shows a significant decrease in peak intensity within the microporous (1–2 nm) and mesoporous (2–5 nm) regions, as partial pores are blocked by PEI modification. BET data analysis (Table S1) shows that the specific surface area of PLB (764.6 m^2/g) is 2.8 times greater than that of PPLB (272.1 m^2/g). This pore blockage phenomenon is consistent with a previous study [32], indicating the

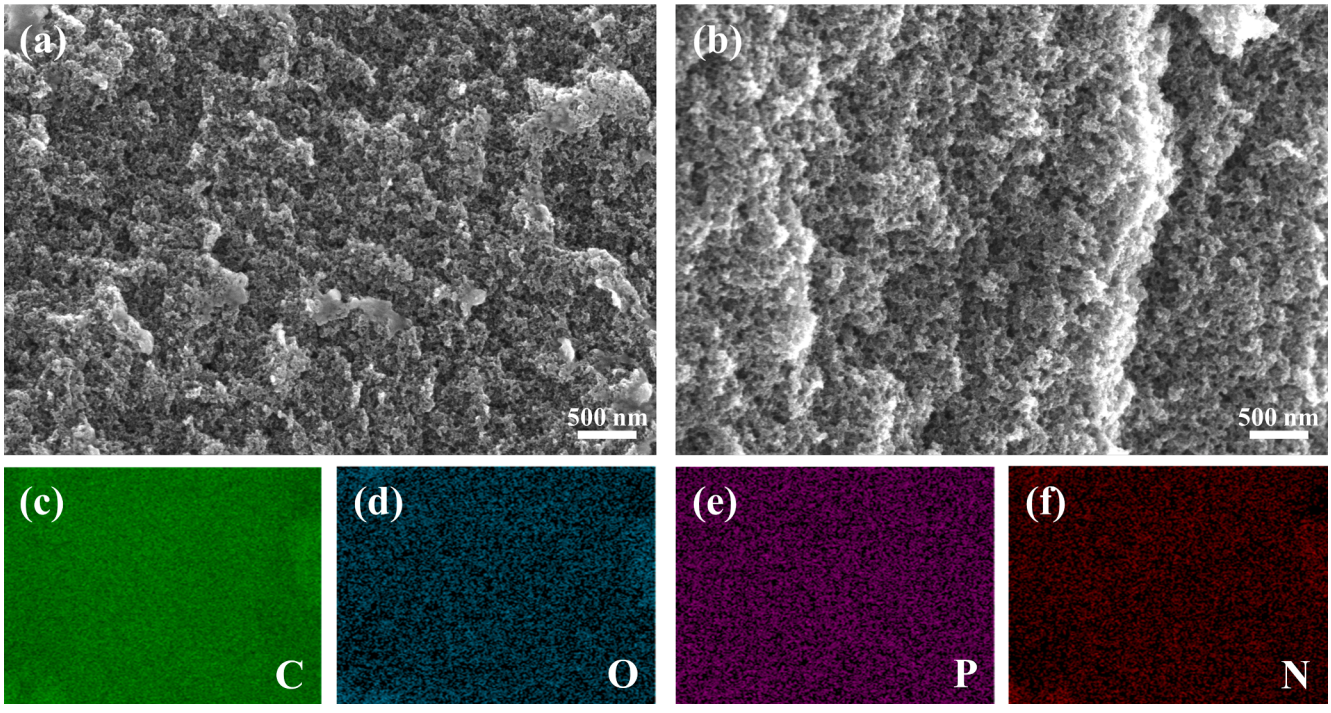

Fig.1. SEM images of PLB (a) and PPLB (b). (c-f) EDS mapping results of elemental carbon (c), oxygen (d), phosphorus (e), and nitrogen (f) of PPLB.

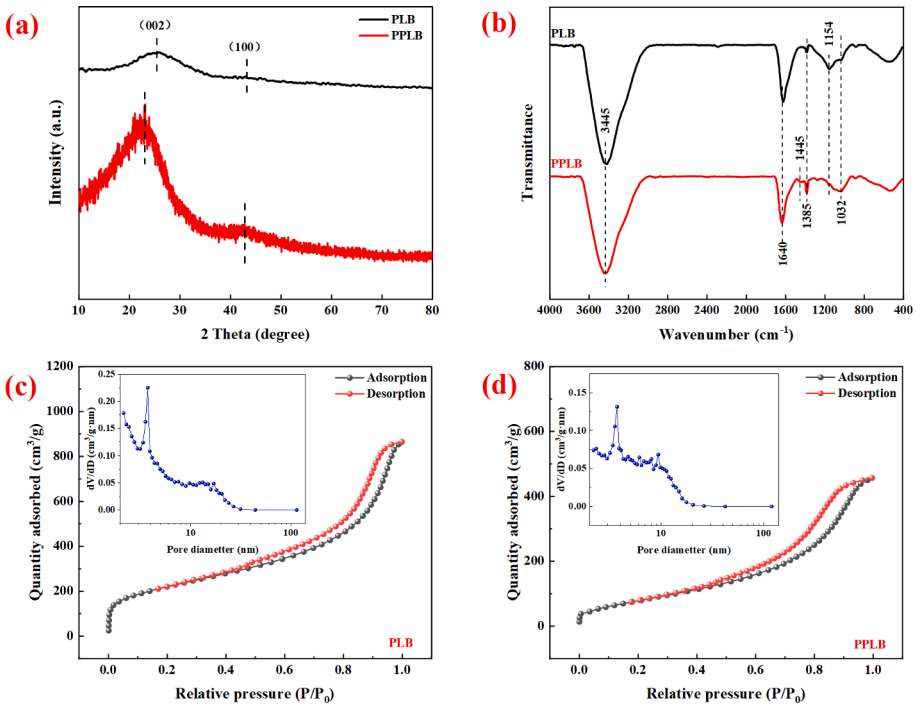

Fig.2. XRD patterns (a) and FTIR spectra (b) of PLB and PPLB. N_2 adsorption–desorption isotherms of PLB (c) and PPLB (d). The insets of (c-d) are the corresponding pore-size distribution.

successful grafting of PEI onto PLB and the formation of a unique hierarchical porous structure.

The surface elemental compositions of PLB and PPLB are further analyzed using XPS. In the overall XPS spectra of PLB and PPLB (Fig. 3a), C, O, and P elements are observed, with no N element detected in PLB. However, a distinct N 1 s peak appears at 400 eV in PPLB, indicating a significant increase in N content from the amino groups in PEI (Fig. 3b). The N 1 s featuring peak is divided into three peaks at 401.8, 400.2, and 399.6 eV, corresponding to –N=, –NH-, and $–NH_2$, respectively [33]. In the C 1 s spectrum of PLB (Fig. 3c), four peaks with binding energy at 284.8, 285.5, 286.6, and 289.3 eV are assigned to C-C, C-N/C-P, C-O, and C=O, separately. With PEI modification, the intensities of the C-N and C-O groups increase, correlating with the grafting method of PEI, in consistent to the above FTIR results (Fig. 2b). In addition, the P 2p spectrum of PLB (Fig. 3d) is divided into three peaks at 132.1, 133.4, and 134.3 eV, which are assigned to C-P=O, C-P-O, and C-O-P, [34] respectively. Additionally, the intensity of the C-P=O peak increases while the C-O-P peak decreases, attributed to the reaction of phosphorus-containing groups with primary and secondary amines of PEI molecules to form phosphoramides or other complex P-N-O groups

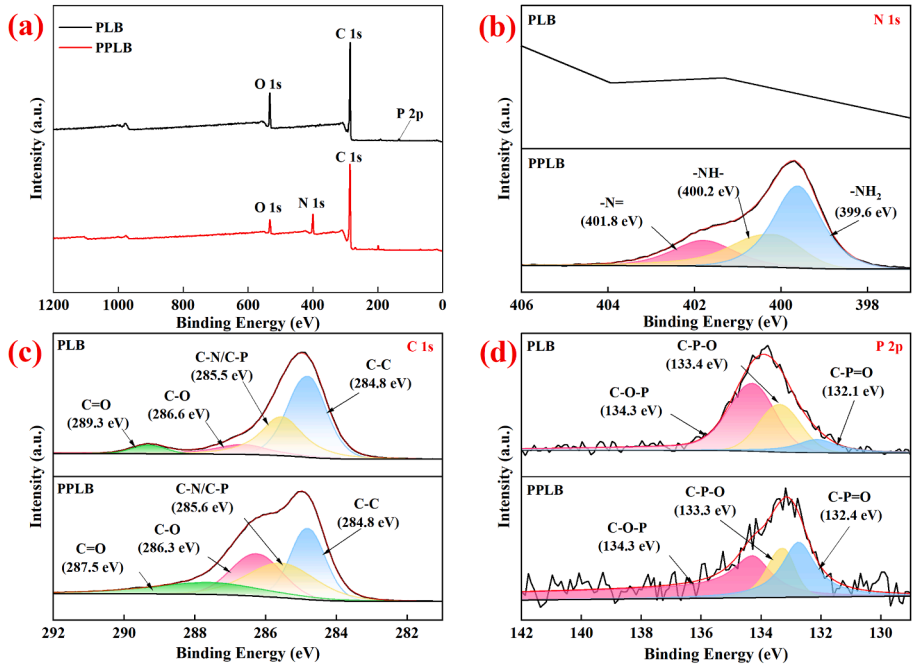

Fig.3. XPS survey spectra (a). N 1 s (b) and C 1 s (c) and P 2p (d) spectra of PLB and PPLB.

[35].

3.2. Antimony removal study

3.2.1. Influence factors of antimony elimination

A range of batch experiments have been conducted to study the key factors, including initial solution pH (pH_0), dosage, and initial Sb(III) concentration ($[Sb(III)]_0$), that govern the removal performance of Sb (III) by the synthetic adsorbents. First, the removal efficiency of Sb(III) by PPLB achieves 85.6 % at pH_0 of 3 after 120 min, in contrast to only about 10 % by PLB (Fig. S2) under the same condition. This suggests that the modification of PEI molecules onto PPLB significantly enhances the adsorption of Sb(III), which is investigated in detail later. As shown in Fig. 4a, the adsorption efficiency and capacity of Sb(III) by PPLB increase from pH_0 of 2 to 3, while decrease sharply from pH_0 of 3 to 8, thus displaying a maximum equilibrium absorption capacity of Sb(III) by PPLB of 180.8 mg/g at pH_0 of 3. This pH-sensitive behavior is further analyzed according to the Pourbaix diagram of Sb (Fig. 4b). Sb(III) is mainly present as $Sb(OH)_3$ molecules in the pH window of 2–8. Meanwhile, the amino groups of PEI on PPLB will be protonated with the formation of species e.g., $–NH_3^+$, $–NH_2^+$-. Combined with the pH_{pzc} value (7.1) of PPLB (Fig. S3), when the $pH_0 < 7.1$, the surface of PPLB is positively charged [36]. Therefore, with the increase of pH_0 from 3 to 8, the decay of Sb(III) removal is mainly due to the decrease in protonation degree of amino groups. Besides, within the pH_0 region of 2–3, there is a slight increase in Sb(III) adsorption efficiency. This observation may be the result of the extra H^+ ions in strongly acidic condition ($pH_0 = 2$) interact with –OH surface groups on PPLB, influencing the effect of hydrogen bonding and ligand exchange between –OH groups of PPLB and $Sb(OH)_3$, thus leading to the slight decrease of Sb(III) adsorption at pH_0 of 2 [11]. Further, the mechanism of good adsorption capability of Sb(III) by PPLB is supposed not limited to electrostatic adsorption, but also due to the complexation between protonated amino groups of PEI and $Sb(OH)_3$ molecules, which will be discussed later. Overall, pH_0 3 is adopted in subsequent investigation.

Fig. 4c illustrates the effect of dosage on the removal performance and adsorption of Sb(III) at $[Sb(III)]_0$ of 50 mg/L and pH_0 of 3. As the dosage increases from 0.05 to 0.15 g/L, both the removal efficiency and adsorption capacity of Sb(III) rise as more adsorption sites are available on PPLB. When the dosage further increases beyond 0.25 g/L, the excessive adsorption sites lead to competitive adsorption, and the pH value of the solution is increased with the increasing dosages of PPLB

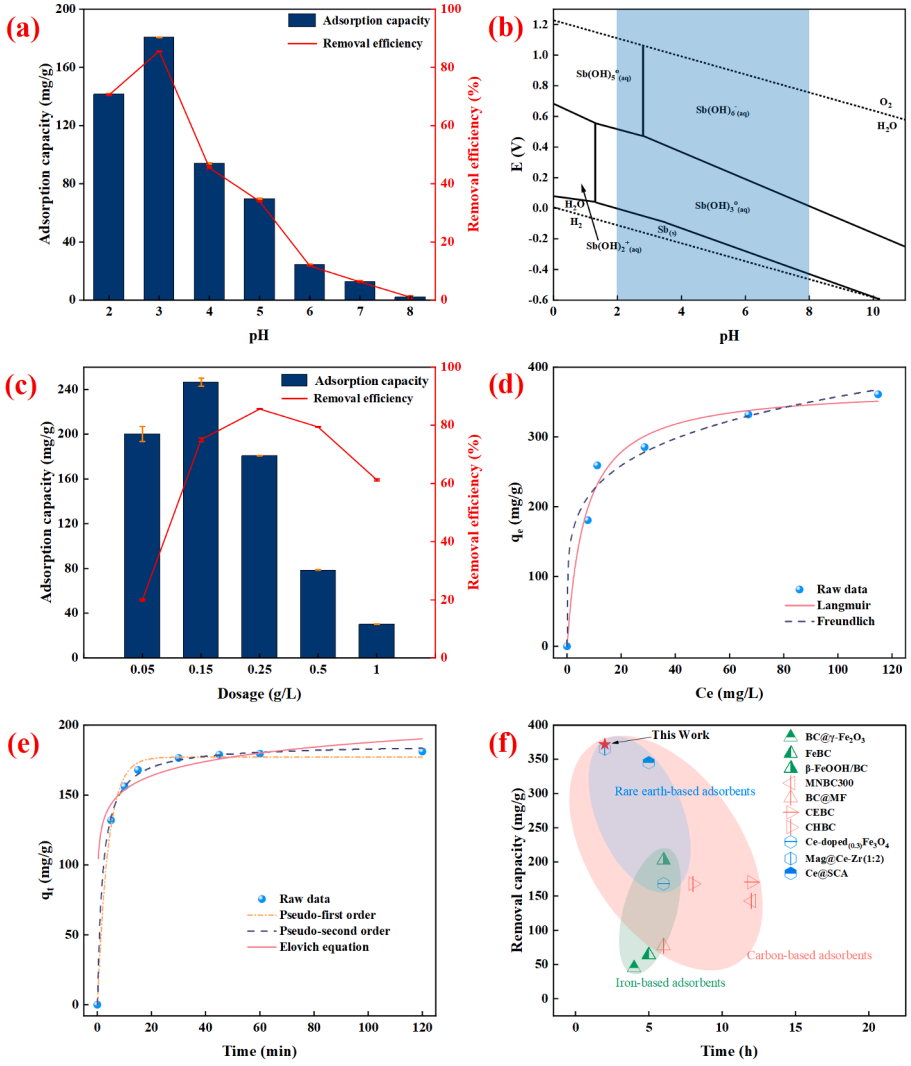

Fig.4. (a) pH effect of the Sb(III) removal by PPLB. (b) Pourbaix diagram of Sb at 25℃. (c) The dosage effect of the Sb(III) elimination by PPLB. (d) The isotherms of Sb(III) elimination onto PPLB fitted with the Langmuir and Freundlich model. (e) Sb(III) elimination kinetics of PPLB, simulated by pseudo-first/second order and Elovich equation. (f) Comparison of removal capacities with iron-based adsorbents (green symbol), carbon-based adsorbents (pink symbol), and rare earth-based adsorbents (blue symbol) towards Sb(III) (where applicable): $[Sb(III)]_0 = 75$ mg/L, $pH_0 = 3 \pm 0.1$, and dose of 0.25 g/L. (For interpretation of the references to colour in this figure legend, the reader is referred to the web version of this article.)

due to the protonation of amino groups, resulting in a decrease in Sb(III) adsorption capacity. At a dosage of 0.15 g/L, the equilibrium removal amount of Sb(III) reaches a maximum of 246.6 mg/g. Additionally, at a dosage of 0.25 g/L, the equilibrium removal amount is 180.8 mg/g, with a maximum removal efficiency of 85.6 %. Considering both adsorption capacity and removal efficiency, a dosage of 0.25 g/L is selected for later study. Fig. S4 demonstrates the effect of the $[Sb(III)]_0$ ranging from 50 to 200 mg/L on the removal of Sb(III) by PPLB. At $[Sb(III)]_0$ of 50 mg/L, the removal efficiency of Sb(III) is determined to be 85.6 %, with an adsorption capacity of 180.8 mg/g. While the removal efficiency and capacity at a higher $[Sb(III)]_0$ of 75 mg/L increase, which are 85.3 % and 259.5 mg/g, respectively. Further increase of $[Sb(III)]_0$ to 200 mg/L witnesses an increased equilibrium removal capacity of 361.2 mg/g, but a decreased removal efficiency of 44 %. Considering both of the above batch experiment results and potential practical applications, the optimal conditions of PPLB adsorbent for further studies are selected to be $pH_0 = 3$, dosage of 0.25 g/L, and $[Sb(III)]_0$ of 75 mg/L.

The isotherms for Sb(III) removal by PPLB are fitted using the Langmuir and Freundlich models (Fig. 4d). Given the coefficient of determination (R^2) fitted from the Langmuir ($R^2 = 0.983$)/Freundlich ($R^2 = 0.983$) model simulations (Table S2) [37], the isotherm for Sb(III) removal by PPLB aligns more closely to the Langmuir model. It suggests that the removal mechanism of Sb(III) by PPLB is more likely to be monolayer adsorption on a uniform surface. The corresponding kinetic curves for Sb(III) removal by PPLB are fitted with pseudo-first-order, pseudo-second-order, and Elovich models (Fig. 4e). The R^2 for the pseudo-second-order model is 0.999, greater than 0.995 for the pseudo-first-order model and 0.986 for the Elovich model, respectively (Table S3). Therefore, the kinetic curve for Sb removal by PPLB is consistent to the pseudo-second-order model, indicating that the primary mechanism is chemisorption. We also use the intra-particle diffusion model to understand the diffusion nature during the adsorption process. The fitted curve does not pass through the origin point (Fig. S5), suggesting that intra-particle diffusion is not the only rate-limiting step and that the adsorption process is controlled by multiple steps [38]. The adsorption process can be grouped into three linear regions. The $k_{int,1}$ (20.90) value fitted for the first stage is higher than those of $k_{int,2}$ (3.14) and $k_{int,3}$ (0.013) (Table S3), indicating the highest adsorption rate, likely due to the diffusion of Sb(III) to the boundary layer on the external surface. In the second region, the intra-particle diffusion becomes the rate-limiting step, as Sb ions gradually occupy the adsorption sites. The third region represents the equilibrium process. Furthermore, compared to other adsorbents for Sb(III) removal (Table S6, and Fig. 4f), the PPLB prepared in this study exhibits a superior Sb(III) removal capability, with a maximum Sb(III) removal capacity of 371.7 mg/g.

3.2.2. *Effect of coexisting ion and reusability*

Antimony ions in natural and industrial wastewater often coexist with various anions such as Cl^-, NO_3^-, CO_3^{2-}, PO_4^{3-}, and SO_4^{2-}. They also compete with antimony ions for adsorption sites on the adsorbent, affecting the removal efficiency [39]. Fig. 5a shows the effect of the coexisting anion on the adsorption of Sb(III) by PPLB. The removal efficiencies of Sb(III) are 86.8 %, 86.4 %, 86.1 %, 87.6 %, and 52.1 %, in different coexisting anions such as Cl^-, NO_3^-, CO_3^{2-}, PO_4^{3-}, and SO_4^{2-}, respectively. Besides, as shown in Fig. S6, when $[PO_4^{3-}]$ are 75, 150, 300 and 600 mg/L, the removal rates of Sb(III) are 82.1 %, 83.8 %, 78.1 % and 75.5 %, respectively. Therefore, the removal efficiency of Sb(III) by PPLB is not greatly affected by the coexistence of PO_4^{3-}. Except of SO_4^{2-}, other common anions do not significantly influence the adsorption of Sb (III). SO_4^{2-} strongly competes with Sb(III) for the active sites of PPLB adsorbent due to its high affinity to amino groups [27].

Antimony is a potential electrode material for SIBs [40]. Selectively enriching antimony from wastewater is the first step to convert spent antimony-enriched adsorbents into sodium storage materials [41]. The selective adsorption performance of Sb(III) with the commonly coexisting metal ions by PPLB is thus investigated [42]. Fig. 5b shows when the concentration ratio of Cd^{2+}, Zn^{2+}, Cu^{2+}, and Pb^{2+} to Sb(III) is 1:1, the adsorption efficiency of antimony reaches 84.9 %, while the adsorption ratios of Cd^{2+}, Zn^{2+}, Cu^{2+}, and Pb^{2+} are only 1.4 %, 1.3 %,

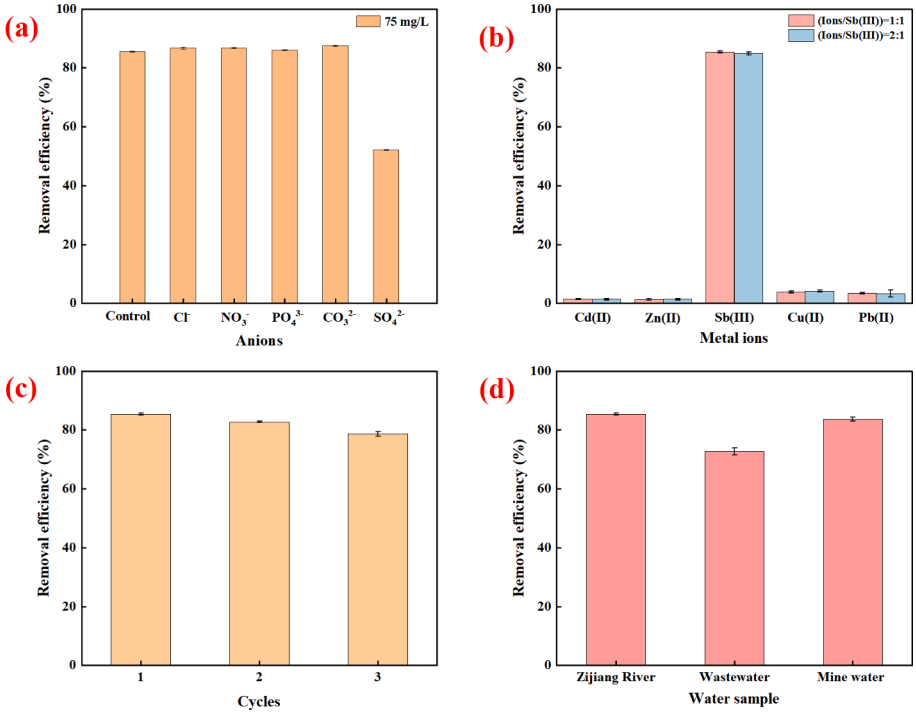

Fig.5. (a) Effects of different competitive anions (Cl^-, NO_3^-, CO_3^{2-}, PO_4^{3-}, and SO_4^{2-}) on the Sb(III) removal by PPLB. (b) Selective adsorption performance of Sb(III) with the coexistence of Cd^{2+}, Zn^{2+}, Cu^{2+}, and Pb^{2+}, respectively. (c) Reusability of Sb(III) removal by PPLB. (d) Comparison of Sb(III) removal performance by PPLB in different water samples (initial concentration of 75 mg/L). $[Sb(III)]_0 = 75$ mg/L, pH_0: 3 ± 0.1, dose: 0.25 g/L, contact time: 2 h.

4.1 %, and 3.3 %, respectively. When the concentration ratio of coexisting ions to Sb(III) is up to 2:1, the results are similar. These results reveal PPLB can selectively enriches antimony without adsorbing these cations. The prepared PPLB adsorbent is expected to meet the potential applicability for selective adsorption of Sb(III) ions from wastewater [43]. To evaluate the reusability of PPLB for Sb(III) removal, Fig. 5c shows the first three consecutive adsorption-regeneration cycles. In the first cycle, PPLB achieves an Sb(III) removal rate of 85.34 %. The spent PPLB is then treated with NaOH for desorption and regenerated by washing with ultrapure water. PPLB maintains an Sb(III) removal efficiency of 78.6 % after three cycles, demonstrating a high stability and reusability. Such a slight decrease is frequently observed in previous reports [4,11]. It's likely due to the decreased number of active sites in PPLB through the washing by NaOH solution, and also the irreversible Sb(III) adsorption occupying the active sites.

3.2.3. *Application of PPLB on selective adsorption of antimony in different water sources*

To evaluate the selective adsorption of antimony by PPLB in different water sources, three water samples are selected, including Zijiang River water [44], industrial wastewater, and mining area water. Detailed compositional analysis of common metal ions (Cd^{2+}, Zn^{2+}, Cu^{2+}, Pb^{2+}, Mn^{2+}, etc.) in the samples is shown in Table S4. No significant antimony contamination is detected in the three samples. As shown in Fig. 5d, the removal rate of Sb(III) ($[Sb(III)]_0$ = 75 mg/L) in pH-adjusted Zijiang River water is approximately 84.5 %, and 82.6 % in pH-adjusted mine area water, indicating a good adsorption performance. The removal efficiency of Sb(III) by PPLB in industrial wastewater shows a declined adsorption performance of 72.7 %, likely due to the competition with other highly concentrated metal cations. Moreover, the PPLB adsorbent demonstrates a selective adsorption of antimony while excluding other metal cations. Besides, $[Sb(III)]_0$ of 10 mg/L with pH_0 = 3 ± 0.1 is chosen to represent the typical real-world water conditions. The removal efficiencies of Sb(III) (Fig. S7a) reach more than 80 % with the addition of 0.05 and 0.15 g/L of the absorbent, much higher than those at $[Sb(III)]_0$ of 75 mg/L (Fig. 4c). The residual Sb(III) in the solution may be assigned to the adsorption–desorption equilibrium on PPLB. Further increase the dosage, the removal efficiency decreases significantly, as also greater changes of the pH of the solution. The increased amount of adsorbent elevates the pH of the solution due to the protonation of the amine group (Fig. S7b), but lowering the removal efficiency of Sb(III).

3.3. *Removal mechanisms*

To further analyze the mechanisms of antimony removal by PPLB, a range of material characterization techniques have been employed. FTIR spectra of PPLB before and after Sb(III) treatment are first analyzed (Fig. 6a). The intensity of the overlapping vibration peak at 3445 cm^{-1} for –OH, $–NH_2$, and –NH- significantly decreases, indicating that $–NH_2$ and –NH- groups from PEI molecules in the composite are the primary adsorption sites for Sb(III). New vibration peaks formed at 740 and 580 cm^{-1} are due to the stretching vibration characteristic peaks of O-Sb [45]. XPS spectra of PPLB (Fig. 6b-d) further reveal changes in surface elemental composition. In Fig. 6b, it is observed that the content of $–NH_2$ decreases from 50.6 % to 38.9 % after Sb(III) treatment, while the content of –N=increases from 22.7 % to 38.9 %. This suggests that primary amino groups may react to form ternary amines, or both primary and secondary amino groups act as adsorption sites for Sb(III). In the C 1 s spectrum (Fig. 6c), the content of C=O decreases from 17.3 % to 12.3 %, with a peak shift, suggesting that –COOH groups on the carbon surface also play a role in Sb(III) adsorption. The O 1 s + Sb 3d spectrum (Fig. 6d) shows the presence of Sb 3d peaks, confirming the adsorption of Sb on the biochar surface. Sb 3d can be divided into Sb $3d_{5/2}$ and Sb $3d_{3/2}$, corresponding to binding energies of 531.5 and 540.5 eV from Sb (III), respectively [46]. Additionally, the XRD patterns of PPLB before and after Sb(III) treatment (Fig. S8) show no significant changes, indicating that the crystallinity of PPLB remains stable during the removal process. In addition, SEM observation at the carbon layer surface reveals no obvious signs of morphology change (Fig. S9a-b). SEM-EDS results (Fig. S9c-f) suggest that the elements of C, Sb, N, O, and P are uniformly distributed on the PPLB-Sb(III) sample.

To further gain the insight of the mechanisms of Sb(III) removal by PPLB, computational simulation is used to study the bonding interaction between amino groups of PEI molecules ($–NH_2$, –NH- and –N=) and Sb

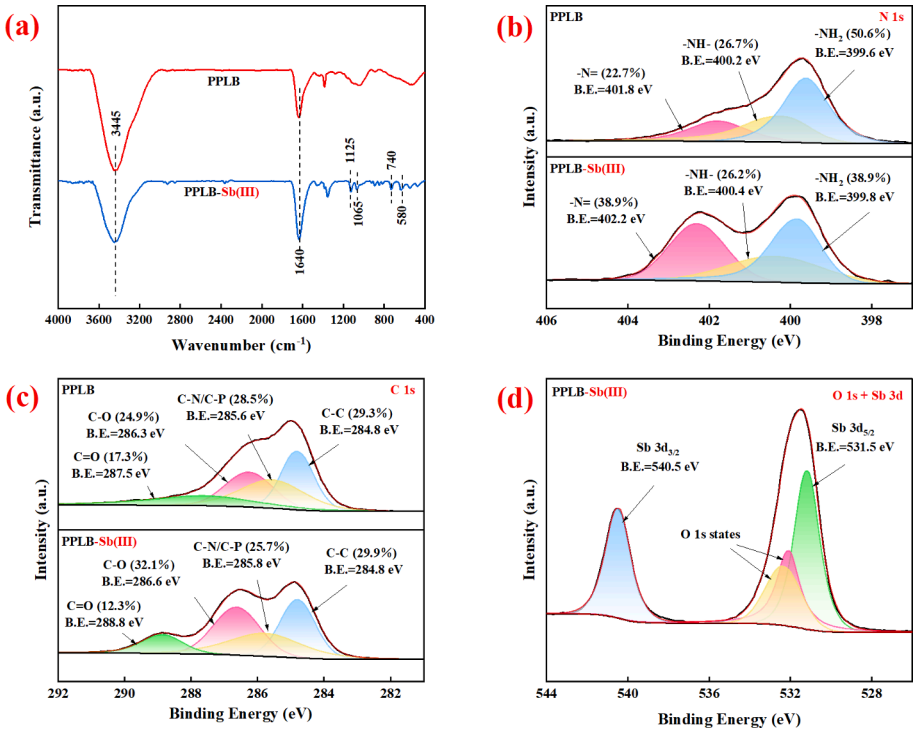

Fig.6. FTIR spectra (a) and XPS spectra (b-d) of PPLB before and after treatment with Sb(III). ($[Sb(III)]_0$ = 75 mg/L, pH_0: 3 ± 0.1, dose: 0.25 g/L, contact time: 2 h).

(III). $Sb(OH)_3$ represents the predominant form of Sb(III) at pH=3 (Fig. 4b), and thus it is thus the primary study object here. Fig. 7 illustrates the DFT modeling results between the binding of a PEI molecular monomer and $Sb(OH)_3$. Three possible adsorption pathways are proposed to compare the energies of complex molecule with the consideration of steric hindrance: (i) a $–NH_2$ group in the PEI molecule binds with $Sb(OH)_3$. (ii) a –NH- group in the PEI molecule binds with $Sb(OH)_3$. (iii) a −N= group in the PEI molecule binds with $Sb(OH)_3$.

As for the three adsorption pathways, the bond lengths of Sb-N in $–NH_2$-Sb(III) and –NH-Sb(III) complexes are 2.275 and 2.276 Å, respectively, while the −N= group does not exhibit binding potential with Sb(III). Thus, $–NH_2$ and –NH- groups can interact with $Sb(OH)_3$, forming stable complexes, with computational molecular energies of −56.75 and −71.63 eV (Table S5), respectively. The more negative of the energy of the computational complex molecule leads to the easier of the formation the corresponding adsorption sites with Sb(III). Therefore, this adsorption pathway from the complexation between –NH- groups and $Sb(OH)_3$ is the most possible for Sb(III) removal. This result is likely explained by the formation of a water molecule (Fig. 7) when one hydroxyl (–OH) of $Sb(OH)_3$ combines with an hydrogen atom from another –OH during the complexation process of –NH- with Sb(III), leading to the generation of Sb-O with a bond length of 1.82 Å, which is lower than bond lengths of Sb-OH (1.94 and 1.96 Å) in $–NH_2$-Sb(III) complex. Overall, $–NH_2$ and –NH- are effective functional groups capable of strong complexation with Sb(III).

The removal mechanisms of Sb(III) by PPLB, including complexation, ligand exchange, and hydrogen bonding, are finally illustrated in Fig. 8. Complexation is dominant for Sb(III) removal. The highly protonated amino groups ($–NH_2$, –NH-) of PEI molecules on PPLB have a strong affinity to the hydroxyl groups of $Sb(OH)_3$ under acidic condition. The DFT simulation reveals a strong binding effect between N and Sb, indicating that amino groups ($–NH_2$, –NH-) can interact with $Sb(OH)_3$ under acidic condition to remove Sb(III) effectively. Meanwhile, functional groups including –OH and –COOH present on the surface of PPLB can also participate in the removal of Sb(III) through hydrogen bonding and ligand exchange.

3.4. Treatment cost and potential reutilization as an electrode material

The cost of the entire synthetic process of adsorbent, including electricity, raw materials and chemicals, is evaluated. The total cost of PPLB is 2.027 USD g^{-1} (Fig. S10). Further, the cost of the modifier is compared with other previously reported adsorbents, which is competitive (Table S7). Meanwhile, The spent PPLB-Sb(III) adsorbent is recycled and converted to Sb/C composite for the secondary use. XRD analysis indicates the presence of a notable crystalline phase of antimony in the Sb/C composite (Fig. S11a). Fig. S11b-d show the cycling performance and rate capability of Sb/C composite as an electrode material or sodium ion batteries. Sb/C composite maintains a specific capacity of 297.8 mA h/g over 100 cycles at a current density of 100 mA/g. Further, it delivers a specific capacity of 192.4 mA h/g over 1000 cycles at a relatively high current density of 500 mA/g, showing a superior long-term stability. Regarding rate performance, Sb/C composite retains specific capacities of 331, 283, 235, 202, and 162 mA h/g at operational current densities of 100, 200, 500, 1000, and 2000 mA/g, respectively. When the current density is reset to 100 mA/g, the capacity of Sb/C recovers to 310 mA h/g, demonstrating that Sb/C composite has a good rate performance. These preliminary results hold a promise that the spent PPLB adsorbed with Sb(III) can be reutilized as a highly-valued electrode material.

4. Conclusion

This study explores the enhancement effect of amino groups on the removal of Sb(III). PEI molecules with numerous amino groups ($–NH_2$, –NH-, and −N=) are grafted onto phosphoric acid-modified lignin-based porous biochar, providing plenty of adsorption sites for Sb(III) removal. PPLB exhibits a maximum Sb(III) removal capacity of 371.7 mg/g, comparable to the state-of-the-art metal-based adsorbents for Sb(III) removal (Fig. 4f). PPLB demonstrates a good Sb(III) removal performance with the coexistence of common anions (Cl^-, NO_3^-, PO_4^{3-}, and CO_3^{2-}) and exhibits an efficient selective adsorption ability of Sb(III) among four cations (Cd^{2+}, Zn^{2+}, Cu^{2+}, and Pb^{2+}) in water. Interestingly, the $–NH_2$ and –NH- groups have strong affinities to Sb(III) by complexation based on the DFT results, with the –NH- group forming a more stable bond with Sb(III). Thus, the removal mechanism of Sb(III) by PPLB are dominated by complexation, with also the contribution from ligand exchange and hydrogen bonding. Further, the Sb(III)-treated adsorbent is converted into a sodium-ion battery anode material, which maintains a specific capacity of 191.4 mA h/g over 1000 cycles with a superior long-term stability. This proof-of-concept work provides a route for the upgrade of spent Sb-containing adsorbents as electrode materials. Future work will focus on (i) evaluation of the remediation of real Sb-contaminated soil by PPLB and (ii) gaining a deeper understanding on the conversion from spent adsorbents into more efficient battery materials.

CRediT authorship contribution statement

Wei Huang: Writing – original draft, Supervision, Investigation,

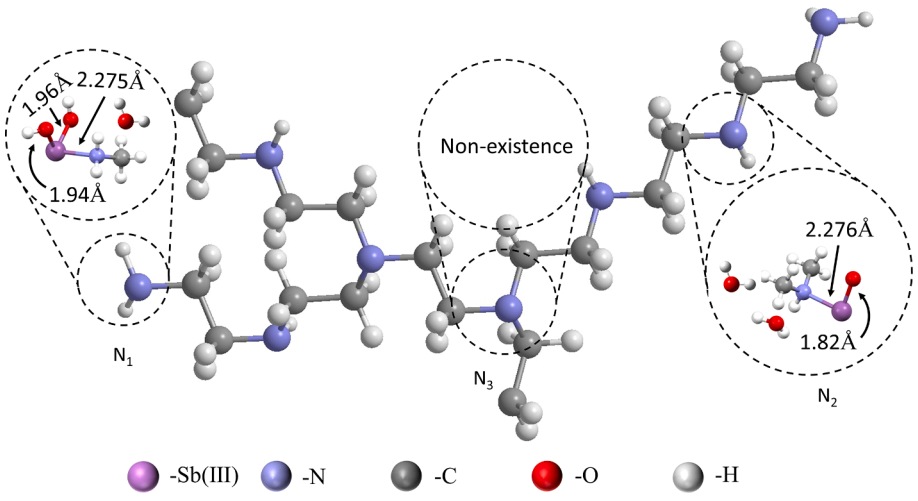

Fig.7. The optimized geometric structure of PEI with the binding energy towards Sb(III), obtained by DFT calculations.

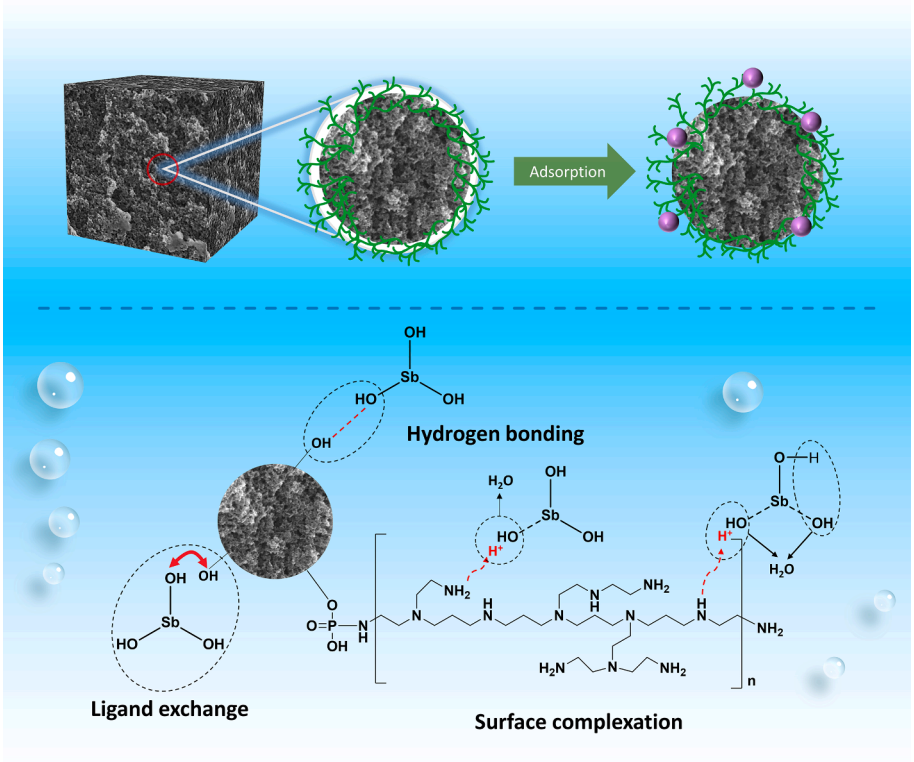

Fig.8. Schematic drawing of Sb(III) removal mechanisms by PPLB.

Formal analysis. **Zhixuan Yang:** Investigation, Formal analysis, Data curation. **Junguang Hu:** Validation, Investigation. **Xin Chen:** Investigation, Data curation. **Wei Li:** Writing – original draft, Supervision, Investigation, Formal analysis. **Zhiguo Wang:** Resources, Investigation. **Chun Zhang:** Resources, Data curation. **Qiongchao Wang:** Resources, Methodology. **Xinxin Xiao:** Writing – review & editing, Methodology, Investigation, Funding acquisition. **Peng Yu:** Writing – review & editing, Supervision, Resources, Funding acquisition.

Declaration of competing interest

The authors declare that they have no known competing financial interests or personal relationships that could have appeared to influence the work reported in this paper.

Data availability

Data will be made available on request.

Acknowledgements

This study was supported by the Hunan Provincial Natural Science Foundation of China (2023JJ40330 & 2023JJ50322), Provincial Science and Technology Project of Nonggao District, Jinggangshan (20222-051245), Research Foundation of Education Bureau of Hunan Province, China (22B0184) and Postgraduate Scientific Research Innovation Project of Hunan Province (CX20240669). X.X. acknowledges a Novo Nordisk Foundation Start Package grant (0081331).

Appendix A. Supplementary data

Supplementary data to this article can be found online at https://doi.org/10.1016/j.cej.2024.156262.

References

[1] L. Peng, N. Wang, T. Xiao, J. Wang, H. Quan, C. Fu, Q. Kong, X. Zhang, A critical review on adsorptive removal of antimony from waters: adsorbent species, interface behavior and interaction mechanism, Chemosphere 327 (2023) 138529, https://doi.org/10.1016/j.chemosphere.2023.138529.

[2] M. Wei, B. Wang, P. Wu, X. Zhang, M. Chen, S. Wang, Electrolytic manganese residue-biochar composite for simultaneous removal of antimony and arsenic from water: adsorption performance and mechanisms, J. Cleaner Prod. 437 (2024) 140623, https://doi.org/10.1016/j.jclepro.2024.140623.

[3] W. Chen, R. Deng, Y. Chen, C. Wang, B. Hou, S. Zhou, A. Hursthouse, New insights into adsorption of As(V) and Sb(V) from aqueous by HCO–(Fe3O4)x adsorbent: adsorption behaviors, competition and mechanisms, J. Water Process Eng. 58 (2024) 104873, https://doi.org/10.1016/j.jwpe.2024.104873.

[4] Y. He, R. Sun, D. Zhang, Y. Wang, S. Zhou, X. Deng, B. Wang, G. Hu, Separable alginate gel spheres encapsulated with La-Fe modified biochar for efficient adsorption of Sb(III) with high capacity, J. Hazard. Mater. 460 (2023) 132322, https://doi.org/10.1016/j.jhazmat.2023.132322.

[5] Z. Cheng, H. Lyu, Y. Huang, B. Shen, J. Tang, Metal cations enhanced the bonding of Sb(V) on adsorbent surfaces: an effective strategy for adsorbent engineering, Chem. Eng. J. 479 (2024) 147630, https://doi.org/10.1016/j.cej.2023.147630.

[6] S. Deng, B. Ren, B. Hou, X. Deng, R. Deng, G. Zhu, S. Cheng, Adsorption of Sb(III) and Pb(II) in wastewater by magnetic γ-Fe2O3-loaded sludge biochar: performance and mechanisms, Chemosphere 349 (2024) 140914, https://doi.org/10.1016/j.chemosphere.2023.140914.

[7] N. Bolan, M. Kumar, E. Singh, A. Kumar, L. Singh, S. Kumar, S. Keerthanan, S. A. Hoang, A. El-Naggar, M. Vithanage, B. Sarkar, H. Wijesekara, S. Diyabalanage, P. Sooriyakumar, A. Vinu, H. Wang, M.B. Kirkham, S.M. Shaheen, J. Rinklebe, K.H. M. Siddique, Antimony contamination and its risk management in complex environmental settings: a review, Environ. Int. 158 (2022) 106908, https://doi.org/10.1016/j.envint.2021.106908.

[8] R. Duan, L. Tian, Y. Liu, Y. Zhang, R. Xu, H. Wang, Mushroom residue derived magnetic hydrochar for antimony removal from wastewater: mechanisms insights and practicality assessment, Sep. Purif. Technol. 343 (2024) 127187, https://doi.org/10.1016/j.seppur.2024.127187.

[9] Z. Chi, S. Ju, X. Liu, F. Sun, Y. Zhu, Graphene oxide supported sulfidated nano zero-valent iron (S-nZVI@GO) for antimony removal: the role of active oxygen species and reaction mechanism, Chemosphere 308 (2022) 136253, https://doi.org/10.1016/j.chemosphere.2022.136253.

[10] Y. Gao, H. Chen, Z. Fang, N.K. Niazi, K. Adusei-Fosu, J. Li, X. Yang, Z. Liu, N. S. Bolan, B. Gao, D. Hou, C. Sun, J. Meng, W. Chen, B.F. Quin, H. Wang, Coupled sorptive and oxidative antimony(III) removal by iron-modified biochar: mechanisms of electron-donating capacity and reactive Fe species, Environ. Pollut. 337 (2023) 122637, https://doi.org/10.1016/j.envpol.2023.122637.

[11] Q. Zeng, J. Li, L. Dai, J. Zhang, T. Zeng, R. Cheng, J. Chen, M. Zhou, H. Hou, Synthesis of hydrophilic sulfur-doped carbon aerogel microspheres and their mechanism of efficient removal of Sb(III) from aqueous solution, Sep. Purif. Technol. 329 (2024) 125032, https://doi.org/10.1016/j.seppur.2023.125032.
[12] B. Du, W. Li, H. Zhu, J. Xu, Q. Wang, X. Shou, X. Wang, J. Zhou, A functional lignin for heavy metal ions adsorption and wound care dressing, Int. J. Biol. Macromol. 239 (2023) 124268, https://doi.org/10.1016/j.ijbiomac.2023.124268.
[13] H. Chen, Y. Gao, A. El-Naggar, N.K. Niazi, C. Sun, S.M. Shaheen, D. Hou, X. Yang, Z. Tang, Z. Liu, H. Hou, W. Chen, J. Rinklebe, M. Pohořelý, H. Wang, Enhanced sorption of trivalent antimony by chitosan-loaded biochar in aqueous solutions: characterization, performance and mechanisms, J. Hazard. Mater. 425 (2022) 127971, https://doi.org/10.1016/j.jhazmat.2021.127971.
[14] P. Bian, B. Gao, J. Zhu, H. Yang, Y. Li, E. Ding, Y. Liu, Y. Liu, S. Wang, W. Shen, Adsorption of chitosan combined with nicotinamide-modified eupatorium adenophorum biochar to Sb3+: application of DFT calculation, Int. J. Biol. Macromol. 240 (2023) 124273, https://doi.org/10.1016/j.ijbiomac.2023.124273.
[15] F. Ma, H. Zhao, X. Zheng, B. Zhao, J. Diao, Y. Jiang, Enhanced adsorption of cadmium from aqueous solution by amino modification biochar and its adsorption mechanism insight, J. Environ. Chem. Eng. 11 (3) (2023) 109747, https://doi.org/10.1016/j.jece.2023.109747.
[16] K. Flores, D.F. Gonzalez, H.M. Morales, A. Mar, S. Garcia-Segura, J.L. Gardea-Torresdey, J.G. Parsons, Amino-modified upcycled biochar achieves selective chromium removal in complex aqueous matrices, J. Environ. Manage. 360 (2024) 121160, https://doi.org/10.1016/j.jenvman.2024.121160.
[17] B. Du, Y. Wang, Q. Zheng, X. Wang, X. Chen, J. Zhou, G. Yang, R.-C. Sun, A novel modified lignin-based adsorbent for removal of malachite green and Pb2+ ions from wastewater, Sep. Purif. Technol. 330 (2024) 125495, https://doi.org/10.1016/j.seppur.2023.125495.
[18] Q. Tang, H. Wu, M. Zhou, D. Yang, Preparation of a new gel-type lignin-based cationic adsorption resin for efficient removal of Ca2+ from aqueous solutions, Int. J. Biol. Macromol. 241 (2023) 124505, https://doi.org/10.1016/j.ijbiomac.2023.124505.
[19] H. Zhang, K. Xue, B. Wang, W. Ren, D. Sun, C. Shao, R. Sun, Advances in lignin-based biosorbents for sustainable wastewater treatment, Bioresour. Technol. 395 (2024) 130347, https://doi.org/10.1016/j.biortech.2024.130347.
[20] C. Li, J. Shen, J. Wang, C. Bao, B. Li, L. Liu, H. Wang, X. Zhang, Highly compressible and macro-porous hydrogels via the synergy of cryogelation and double-network for efficient removal of Cr(VI), Int. J. Biol. Macromol. 238 (2023) 124160, https://doi.org/10.1016/j.ijbiomac.2023.124160.
[21] Y. He, J. Chen, J. Lv, Y. Huang, S. Zhou, W. Li, Y. Li, F. Chang, H. Zhang, T. Wågberg, G. Hu, Separable amino-functionalized biochar/alginate beads for efficient removal of Cr(VI) from original electroplating wastewater at room temperature, J. Cleaner Prod. 373 (2022) 133790, https://doi.org/10.1016/j.jclepro.2022.133790.
[22] Q. Wang, Y. Tian, L. Kong, J. Zhang, W. Zuo, Y. Li, G. Cai, A novel 3D superelastic polyethyleneimine functionalized chitosan aerogels for selective removal of Cr(VI) from aqueous solution: performance and mechanisms, Chem. Eng. J. 425 (2021) 131722, https://doi.org/10.1016/j.cej.2021.131722.
[23] M. Wang, Y. Chen, Y. Zhang, K. Zhao, X. Feng, Selective removal of Cr(VI) by tannic acid and polyethyleneimine modified zero-valent iron particles with air stability, J. Hazard. Mater. 458 (2023) 132018, https://doi.org/10.1016/j.jhazmat.2023.132018.
[24] Y. Zhang, M. Haris, L. Zhang, C. Zhang, T. Wei, X. Li, Y. Niu, Y. Li, J. Guo, X. Li, Amino-modified chitosan/gold tailings composite for selective and highly efficient removal of lead and cadmium from wastewater, Chemosphere 308 (2022) 136086, https://doi.org/10.1016/j.chemosphere.2022.136086.
[25] G. Kresse, J. Hafner, Ab initiomolecular dynamics for liquid metals, Physical Review B 47 (1) (1993) 558–561, https://doi.org/10.1103/PhysRevB.47.558.
[26] G. Kresse, J. Hafner, Ab initiomolecular-dynamics simulation of the liquid-metal–amorphous-semiconductor transition in germanium, Physical Review B 49 (20) (1994) 14251–14269, https://doi.org/10.1103/PhysRevB.49.14251.
[27] S. Chen, J. Wang, Z. Wu, Q. Deng, W. Tu, G. Dai, Z. Zeng, S. Deng, Enhanced Cr(VI) removal by polyethylenimine- and phosphorus-codoped hierarchical porous carbons, J. Colloid Interface Sci. 523 (2018) 110–120, https://doi.org/10.1016/j.jcis.2018.03.057.
[28] J.D. Akoto, F. Chai, E. Repo, Z. Yang, D. Wang, F. Zhao, Q. Liao, L. Chai, Polyethyleneimine stabilized nanoscale zero-valent iron-magnetite (Fe3O4@nZVI-PEI) for the enhanced removal of arsenic from acidic aqueous solution: performance and mechanisms, J. Environ. Chem. Eng. 10 (6) (2022) 108589, https://doi.org/10.1016/j.jece.2022.108589.
[29] S. Mantovani, S. Khaliha, L. Favaretto, C. Bettini, A. Bianchi, A. Kovtun, M. Zambianchi, M. Gazzano, B. Casentini, V. Palermo, M. Melucci, Scalable synthesis and purification of functionalized graphene nanosheets for water remediation, Chem. Commun. 57 (31) (2021) 3765–3768, https://doi.org/10.1039/d1cc00704a.
[30] K. Su, G. Hu, T. Zhao, H. Dong, Y. Yang, H. Pan, Q. Lin, The ultramicropore biochar derived from waste distiller's grains for wet-process phosphoric acid purification: removal performance and mechanisms of Cr(VI), Chemosphere 349 (2024) 140877, https://doi.org/10.1016/j.chemosphere.2023.140877.
[31] A.I. Rasee, E. Awual, A.I. Rehan, M.S. Hossain, R.M. Waliullah, K.T. Kubra, M. C. Sheikh, M.S. Salman, M.N. Hasan, M.M. Hasan, H.M. Marwani, A. Islam, M. A. Khaleque, M.R. Awual, Efficient separation, adsorption, and recovery of Samarium(III) ions using novel ligand-based composite adsorbent, Surf. Interfaces 41 (2023) 103276, https://doi.org/10.1016/j.surfin.2023.103276.
[32] Y. Yan, Q. An, Z. Xiao, W. Zheng, S. Zhai, Flexible core-shell/bead-like alginate@PEI with exceptional adsorption capacity, recycling performance toward batch and column sorption of Cr(VI), Chem. Eng. J. 313 (2017) 475–486, https://doi.org/10.1016/j.cej.2016.12.099.
[33] M.G. Olayo, E.J. Alvarado, M. González-Torres, L.M. Gómez, G.J. Cruz, Quantifying amines in polymers by XPS, Polym. Bull. 81 (3) (2023) 2319–2328, https://doi.org/10.1007/s00289-023-04829-y.
[34] Z. Bi, L. Huo, Q. Kong, F. Li, J. Chen, A. Ahmad, X. Wei, L. Xie, C.-M. Chen, Structural evolution of phosphorus species on graphene with a stabilized electrochemical interface, ACS Appl. Mater. Interfaces 11 (12) (2019) 11421–11430, https://doi.org/10.1021/acsami.8b21903.
[35] C. Wang, L. Sun, Y. Zhou, P. Wan, X. Zhang, J. Qiu, P/N co-doped microporous carbons from H3PO4-doped polyaniline by in situ activation for supercapacitors, Carbon 59 (2013) 537–546, https://doi.org/10.1016/j.carbon.2013.03.052.
[36] P. Yu, J. Xing, J. Tang, Z. Wang, C. Zhang, Q. Wang, X. Xiao, W. Huang, Polyethyleneimine-modified iron-doped birnessite as a highly stable adsorbent for efficient arsenic removal, J. Colloid Interface Sci. 661 (2024) 164–174, https://doi.org/10.1016/j.jcis.2024.01.163.
[37] Y. Wang, L. Kong, M. He, C. Lin, W. Ouyang, X. Liu, X. Peng, Mechanistic insights into Sb(III) and Fe(II) co-oxidation by oxygen and hydrogen peroxide: dominant reactive oxygen species and roles of organic ligands, Water Res. 242 (2023) 120296, https://doi.org/10.1016/j.watres.2023.120296.
[38] P. Yu, J. Tan, Z. Wang, C. Zhang, Q. Wang, K. Zhu, C. Peng, X. Xiao, W. Huang, Enhanced electron transfer pathway of zero-valent iron particles immobilized on coconut shell derived carbon for prolonged Cr(VI) removal, Colloids Surf., A 682 (2024) 132863, https://doi.org/10.1016/j.colsurfa.2023.132863.
[39] Q. Cheng, Q. Li, X. Huang, X. Li, Y. Wang, W. Liu, Z. Lin, The high efficient Sb(III) removal by cauliflower like amorphous nanoscale zero-valent iron (A-nZVI), J. Hazard. Mater. 436 (2022) 129056, https://doi.org/10.1016/j.jhazmat.2022.129056.
[40] Z. Yang, Q.-L. Kang, W. Rui, L.-J. Yan, X.-H. Meng, T.-L. Ma, Structural engineering of Sb-based electrode materials to enhance advanced sodium-ion batteries, Rare Met. (2024), https://doi.org/10.1007/s12598-024-02730-9.
[41] Y. Wang, X. Zhang, N. Ju, H. Jia, Z. Sun, J. Liang, R. Guo, D. Niu, H.-B. Sun, High capacity adsorption of antimony in biomass-based composite and its consequential utilization as battery anode, J. Environ. Sci. 126 (2023) 211–221, https://doi.org/10.1016/j.jes.2022.05.050.
[42] S. Deng, B. Ren, B. Hou, R. Deng, S. Cheng, Antimony-complexed heavy metal wastewater in antimony mining areas: source, risk and treatment, Environ. Technol. Innovation 32 (2023) 103355, https://doi.org/10.1016/j.eti.2023.103355.
[43] M.R. Awual, M.N. Hasan, M.M. Hasan, M.S. Salman, M.C. Sheikh, K.T. Kubra, M. S. Islam, H.M. Marwani, A. Islam, M.A. Khaleque, R.M. Waliullah, M.S. Hossain, A. I. Rasee, A.I. Rehan, M.E. Awual, Green and robust adsorption and recovery of Europium(III) with a mechanism using hybrid donor conjugate materials, Sep. Purif. Technol. 319 (2023) 124088, https://doi.org/10.1016/j.seppur.2023.124088.
[44] H. Liu, G. Sun, M. He, X. Feng, C. Lin, W. Ouyang, X. Liu, The composition and differences of antimony isotopic in sediments affected by the world's largest antimony deposit zone, Water Res. 254 (2024) 121427, https://doi.org/10.1016/j.watres.2024.121427.
[45] H. Chen, Y. Gao, J. Li, C. Sun, B. Sarkar, A. Bhatnagar, N. Bolan, X. Yang, J. Meng, Z. Liu, H. Hou, J.W.C. Wong, D. Hou, W. Chen, H. Wang, Insights into simultaneous adsorption and oxidation of antimonite [Sb(III)] by crawfish shell-derived biochar: spectroscopic investigation and theoretical calculations, Biochar 4 (1) (2022), https://doi.org/10.1007/s42773-022-00161-2.
[46] D. You, H. Shi, L. Yang, P. Shao, K. Yin, H. Wang, S. Luo, X. Luo, Tuning the Sb(V) adsorption performance of La-MOFs via ligand engineering effect: combined experiments with theoretical calculations, Chem. Eng. J. 435 (2022) 134874, https://doi.org/10.1016/j.cej.2022.134874.